

Reaction-Induced Formation of Stable Mononuclear Cu(I)Cl Species on Carbon for Low-Footprint Vinyl Chloride Production

Dario Faust Akl, Georgios Giannakakis, Andrea Ruiz-Ferrando, Mikhail Agrachev, Juan D. Medrano-García, Gonzalo Guillén-Gosálbez, Gunnar Jeschke, Adam H. Clark, Olga V. Safonova, Sharon Mitchell, Núria López, and Javier Pérez-Ramírez*

Copper catalysts are attractive candidates for Hg-free vinyl chloride monomer (VCM) production via acetylene hydrochlorination due to their non-toxic nature and high stability. However, the optimal architecture for Cu-based catalysts at the nanoscale is not yet fully understood. To address this gap, the metal precursor and the annealing temperature are modified to prepare copper nanoparticles or single atoms, either in chlorinated or ligand-free form, on an unmodified carbon support. Evaluation in the reaction reveals a remarkable convergence of the performance of all materials to the stable VCM productivity of the single-atom catalyst. In-depth characterization by advanced microscopy, quasi in situ and operando spectroscopy, and simulations uncover a reaction-induced formation of low-valent, single atom Cu(I)Cl site motif, regardless of the initial nanostructure. Various surface oxygen groups promote nanoparticle redispersion by stabilizing single-atom CuCl_x species. The anchoring site structure does not strongly influence the acetylene adsorption energy or the crucial role they play in stabilizing key reaction intermediates. A life-cycle assessment demonstrates the potential environmental benefits of copper catalysts over state-of-the-art alternatives. This work contributes to a better understanding of optimal metal speciation and highlights the sustainability of Cu-based catalysts for VCM production.

1. Introduction

The manufacture of vinyl chloride monomer (VCM) via acetylene hydrochlorination, which accounts for 35% of global poly(vinyl chloride) output,^[1] relies on activated carbon-supported mercuric chloride catalysts.^[2,3] Given the toxicity of the compounds emitted due to mercury volatilization during operation,^[4] the pressing search for alternative technologies has prompted many research efforts, wherein catalytic descriptors derived from observed structure–performance relationships were instrumental for improved material design.^[5] An early example was the standard electrode potential of late transition-metal chlorides that placed carbon-supported gold catalysts at the top of the initial VCM productivity ranking, initiating extensive investigation of this metal.^[2,6] The preparation of carbon-supported AuCl₃ strongly impacts catalytic activity because it determines whether active atomically isolated Au(I)Cl

D. Faust Akl, G. Giannakakis, J. D. Medrano-García, G. Guillén-Gosálbez, S. Mitchell, J. Pérez-Ramírez
Institute of Chemical and Bioengineering
Department of Chemistry and Applied Biosciences
ETH Zurich
Vladimir-Prelog-Weg 1–5, Zurich 8093, Switzerland
E-mail: jpr@chem.ethz.ch

A. Ruiz-Ferrando, N. López
Institute of Chemical Research of Catalonia (ICIQ)
Av. Països Catalans 16, Tarragona 43007, Spain

A. Ruiz-Ferrando
Department of Physical and Inorganic Chemistry
Universitat Rovira i Virgili
Marcel·lí Domingo s/n, Tarragona 43007, Spain
M. Agrachev, G. Jeschke
Laboratory of Physical Chemistry
Department of Chemistry and Applied Biosciences
ETH Zurich
Vladimir-Prelog-Weg 1–5, Zurich 8093, Switzerland

A. H. Clark, O. V. Safonova
Paul Scherrer Institute
Forschungsstrasse 111, Villigen PSI 5232, Switzerland

The ORCID identification number(s) for the author(s) of this article can be found under <https://doi.org/10.1002/adma.202211464>

© 2023 The Authors. Advanced Materials published by Wiley-VCH GmbH. This is an open access article under the terms of the Creative Commons Attribution-NonCommercial License, which permits use, distribution and reproduction in any medium, provided the original work is properly cited and is not used for commercial purposes.

DOI: 10.1002/adma.202211464

species or inactive Au nanoparticles form.^[7] Because of the tendency of Au(I)Cl species to aggregate into metallic Au nanoparticles, and the subsequent drastic deactivation of the catalyst, synthetic strategies were devised to stabilize atomically dispersed gold, for example, by anchoring the metal to N-containing defects introduced into the carbon support^[8] or through the use of sulfur-containing gold precursors.^[2]

Concurrently, advances in characterization techniques and the development of synthetic routes for the preparation of single-atom catalysts (SACs)^[9,10] on carbon supports enabled unprecedented control over the metal nuclearity, which highlighted the limitations of the standard electrode potential as an indicator of acetylene hydrochlorination performance, since it had not accounted for the impact of the nanoscale properties. As understanding of these effects deepened, the acetylene binding energy was identified as an improved descriptor for the initial catalyst activity that considered nuclearity and speciation effects over all noble and platinum group metals (PGM), that is, single atoms or nanoparticles on different carbon supports.^[11] The obtained insights permitted individual tailoring of the metal nanoarchitecture for each catalytic system, for example, graphene-covered oxychloride clusters for ruthenium,^[12] surface oxygen-bound isolated atoms for platinum,^[13] or nitrogen-anchored isolated atoms for gold.^[8] Although PGM-based catalysts often suffer from deactivation, attributed to coking or nuclearity changes of metal sites, the optimal choice of physicochemical properties of the carbon support^[14] and synergistic effects in bimetallic systems (e.g., Au–Pt)^[15] improved catalyst longevity. Nonetheless, using scarce and expensive metals, typically exhibiting large carbon footprints, motivates the development of more environmentally benign alternatives.

As an earth-abundant metal, copper catalysts are attractive due to the generally high stability observed in acetylene hydrochlorination (Figure 1 and Table S1, Supporting Information).^[16] However, they tend to exhibit lower activity compared to the best reported Au^[9] and Pt-based systems,^[14] prompting efforts to boost productivity. The most common approaches included increasing the Cu content (up to 25 wt%)^[5] and introducing modifiers either as dopants within the support or co-deposited together with copper on the surface (e.g., P,^[17] Cs,^[18] and ionic liquids^[19]), with almost all studies using activated carbon supports. Such synthetic strategies however often resulted in heterogeneous copper speciation (mixed nuclearity, nonuniform composition) that poses challenges for identifying the optimal active site structure. Based on a comparative analysis (Figure 1 and Table S1, Supporting Information), the impact of the proposed promotional strategies on catalyst activity and stability is unclear. Furthermore, the influence of structural properties and their potential evolution under reaction conditions, critical in developing active and stable PGM catalysts,^[8,11–13] have not been addressed systematically. For instance, the exclusive use of ex situ analyses to assess the electronic state of copper may be subject to erroneous interpretation due to the oxophilicity of the metal. Instead, more suitable characterization approaches (e.g., under in situ or operando conditions)^[20–22] are required but have not been explored thus far (Table S1, Supporting Information). As a result, in some instances, both copper nanoparticles and single atoms have been reported to be optimal nanostructures.^[23,24] Overall, the lack of fundamental understanding of the structure and evolution of

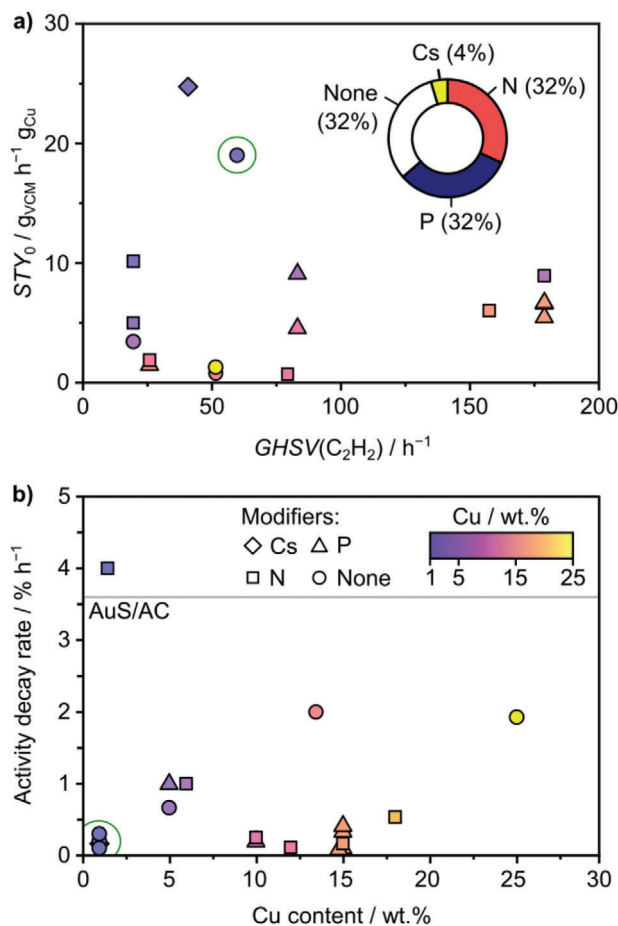


Figure 1. a) Initial space–time yield (STY₀) on a per-metal basis as a function of gas-hourly space velocity of acetylene (GHSV(C₂H₂)). Type and prevalence of catalyst modifiers (in % of studies) shown in the inset and b) activity decay rates estimated through linear approximation from the reported performance data as a function of Cu content. The gray line corresponds to the state-of-the-art carbon-supported gold catalysts (AuS/AC) shown for ref. [3] and the legend in (b) applies to (a). The green circle highlights the CuCl_{SA}/AC catalyst developed in this study (see below).

copper active sites at the atomic scale is a major roadblock toward the targeted development and improvement of environmentally benign Cu-based catalytic systems.

Here, we study copper catalysts with well-defined initial architectures (nanoparticles and single atoms of different speciation) and relatively low metal content (1 wt%) supported on a commercial activated carbon with suitable physicochemical properties for acetylene hydrochlorination.^[14] Evaluation of their performance in acetylene hydrochlorination reveals that the productivity converges to a similar and stable value, among the highest reported in the literature, irrespective of the initial copper nanostructure. The dynamic catalyst evolution is uncovered by quasi in situ and operando X-ray absorption spectroscopy (XAS), electron paramagnetic resonance (EPR), and scanning transmission electron microscopy (STEM) suggesting the redistribution of nanoparticles and transformation of single atoms into a common structural motif. Density functional theory (DFT) simulations indicate that the strong interaction of copper with

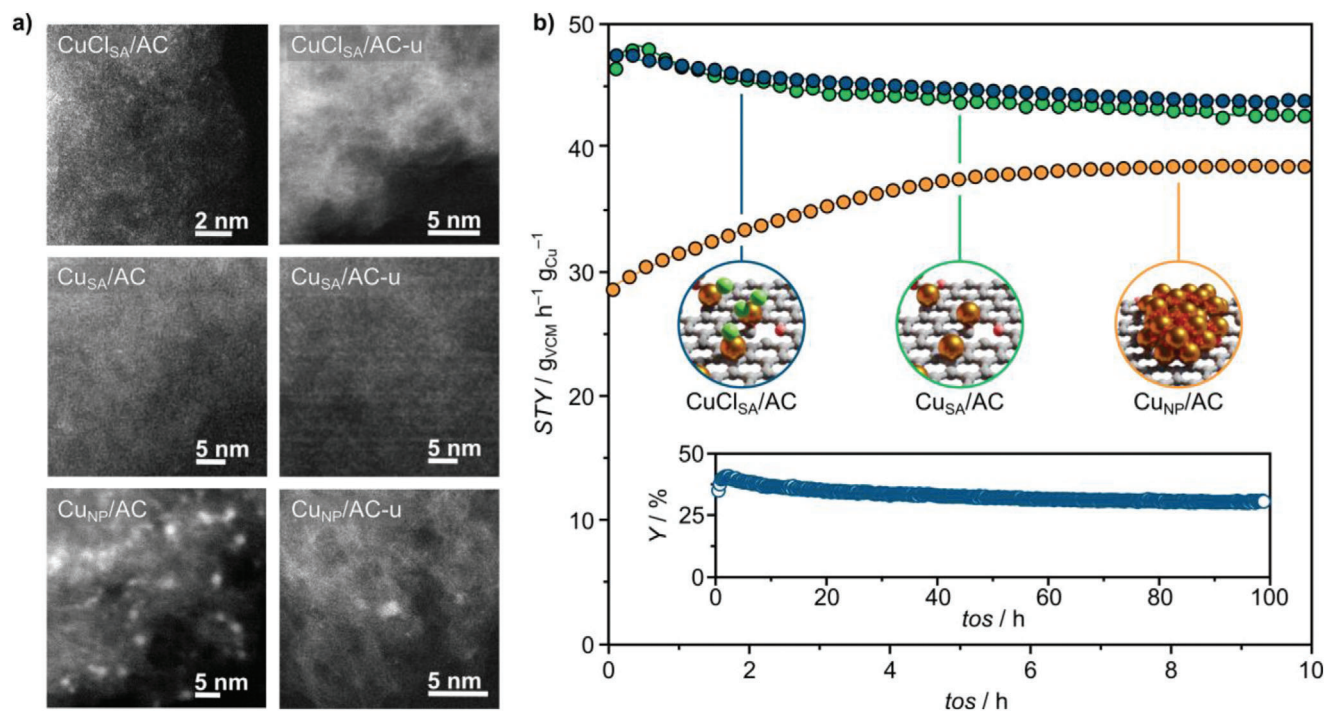


Figure 2. a) (AC)-STEM images of the as-prepared and used (-u, 10 h run) copper catalysts evaluated in this work. b) STY of the Cu-based catalysts in a 10 h run. Conditions: $W_{\text{cat}} = 0.2 \text{ g}$, $F_{\text{T}} = 15 \text{ cm}^3 \text{ min}^{-1}$, $T = 473 \text{ K}$, $\text{GHSV}(\text{C}_2\text{H}_2) = 670 \text{ h}^{-1}$, $\text{HCl}:\text{C}_2\text{H}_2 = 1.1$. The inset shows the yield of VCM during a 100 h under industrially relevant conditions ($W_{\text{cat}} = 1.2 \text{ g}$, $F_{\text{T}} = 10 \text{ cm}^3 \text{ min}^{-1}$, $T = 473 \text{ K}$, $\text{GHSV}(\text{C}_2\text{H}_2) = 70 \text{ h}^{-1}$, $\text{HCl}:\text{C}_2\text{H}_2 = 1.2$).^[16] Color code: carbon, gray; oxygen, red; chlorine, green; copper, orange.

common surface-oxygen groups on the carbon support originates the formation of atomically dispersed CuCl_x sites. DFT-derived reaction profiles further corroborated the identification of $\text{Cu}(\text{I})\text{Cl}$ as active and stable species. A quantitative life-cycle assessment (LCA) embeds the presented $\text{CuCl}(\text{I})$ SAC within the ecosystem of state-of-the-art Au- or Pt-based systems and commercial mercury chloride catalysts showing that despite its moderate activity, the use of earth-abundant copper can deliver tangible environmental benefits.^[25]

2. Results and Discussion

2.1. Impact of Copper Nanostructure in Acetylene Hydrochlorination

To elucidate the effect of the metal nuclearity and speciation on the acetylene hydrochlorination performance, catalysts with distinct initial copper architectures comprising chlorinated ($\text{CuCl}_{\text{SA}}/\text{AC}$) or chlorine-free ($\text{Cu}_{\text{SA}}/\text{AC}$) single atoms, or metal nanoparticles ($\text{Cu}_{\text{NP}}/\text{AC}$) were prepared by a wet impregnation approach varying the metal precursor (i.e., chloride or nitrate) and the annealing temperature (i.e., 473 or 873 K), respectively. Herein, a low nominal metal content (1 wt%) was chosen to promote precise control over the initial structure. The physicochemical properties of the activated carbon support, which was selected based on its promising reported performance for acetylene hydrochlorination and activated by acid treatment to ensure the removal of any impurities, have been described in detail elsewhere.^[14,26] Aberration-corrected annular dark-field scanning

transmission electron microscopy (AC-STEM) images of the as-prepared catalysts confirmed the respective presence of isolated Cu atoms in both SACs and nanoparticles of $\approx 2 \text{ nm}$ diameter in $\text{Cu}_{\text{NP}}/\text{AC}$ (Figure 2a). Consistently, features associated with crystalline metal aggregates were detected in the X-ray diffraction (XRD) pattern of $\text{Cu}_{\text{NP}}/\text{AC}$ but not in those of $\text{CuCl}_{\text{SA}}/\text{AC}$ or $\text{Cu}_{\text{SA}}/\text{AC}$ (Figure S1, Supporting Information).

Ex situ analyses of the electronic properties by X-ray photoelectron spectroscopy (XPS, Figure S2, Supporting Information) and X-ray absorption near-edge structure (XANES, Table S2 and Figure S3, Supporting Information) revealed a $\text{Cu}(\text{II})$ -like oxidation state in both SACs, agreeing with previous reports.^[27] Analysis of the surface composition confirmed the presence or absence of Cl in $\text{CuCl}_{\text{SA}}/\text{AC}$ and $\text{Cu}_{\text{SA}}/\text{AC}$, respectively (Table S3, Supporting Information). Fitting of the extended X-ray absorption fine structure verified the exclusive coordination with support oxygen defects, the presence of chloride ligands in $\text{CuCl}_{\text{SA}}/\text{AC}$, and the absence of long-range scattering peaks characteristic of metal aggregates (EXAFS, Figure S3 and Table S4, Supporting Information). Complementary analysis by continuous wave electron paramagnetic resonance (CW-EPR) spectra of the $\text{CuCl}_{\text{SA}}/\text{AC}$ sample showed typical features for spatially isolated $\text{Cu}(\text{II})$ centers without broad and poorly structured peaks that would be expected in the presence of Cu aggregates or CuO particles (Figures S4 and S5 and Table S5, Supporting Information). Comparatively, XANES (Figure S3, Supporting Information) and XPS (Figure S2, Supporting Information) analysis of $\text{Cu}_{\text{NP}}/\text{AC}$ evidenced predominantly $\text{Cu}(\text{I})$ or $\text{Cu}(\text{II})$ character, suggestive of partial oxidation of the copper nanoparticles due to

exposure to air. The EXAFS (Figure S3, Supporting Information) and (Figure S4, Supporting Information) spectra of Cu_{NP}/AC supported the presence of surface-oxidized Cu nanoparticles. Overall, these results confirmed the obtainment of the desired copper nanostructures covering single atoms of distinct speciation and metal nanoparticles.

The acetylene hydrochlorination performance of the copper catalysts was evaluated at a higher gas-hourly space velocity ($\text{GHSV}(\text{C}_2\text{H}_2) = 670 \text{ h}^{-1}$) than typically studied for Cu-based systems to facilitate comparison with precious metal catalysts (Table S1, Supporting Information).^[11] The initial catalyst space-time yield (STY₀) of CuCl_{SA}/AC was similar to Cu_{SA}/AC ($47.6 \text{ g}_{\text{VCM}} \text{ h}^{-1} \text{ g}_{\text{Cu}}^{-1}$), and both surpassed that of Cu_{NP}/AC (Figure 2b). With progressing time on stream, both SACs displayed a moderate decrease in activity over the first 2 h before equilibrating to a constant STY ($42.4\text{--}43.6 \text{ g}_{\text{VCM}} \text{ h}^{-1} \text{ g}_{\text{Cu}}^{-1}$ after 10 h). In contrast, the STY of the Cu_{NP}/AC catalyst increased from 28.7 to $38.4 \text{ g}_{\text{VCM}} \text{ h}^{-1} \text{ g}_{\text{Cu}}^{-1}$ in the first 6 h approaching the activity level of the SACs.

To gain insights into the convergence of the catalytic performance, the used catalysts were characterized by various complementary ex situ (see Figure S3 and Tables S2 and S4 and S5, Supporting Information), and operando techniques (see below). AC-STEM images of the used catalysts (Cu_{SA}/AC-u and CuCl_{SA}/AC-u) revealed that the atomically dispersed copper species were preserved after the reaction (Figure 2a). Comparatively, the Cu nanoparticles in Cu_{NP}/AC underwent an extensive structural transformation into small clusters and single atoms as illustrated by AC-STEM (Figure 2a), and corroborated through XRD (Figure S1, Supporting Information), ex situ EXAFS (Figure S3, Supporting Information), and ex situ CW-EPR spectroscopy (Figures S4 and S5, Supporting Information).

Because of the inferior activity of Cu_{NP}/AC and the limited impact of the copper speciation on catalyst performance, we focused further assessment on CuCl_{SA}/AC. This catalyst displayed kinetics with partial reaction orders of 0.6 and 0.2 for acetylene and hydrogen chloride, respectively (Figure S6, Supporting Information). The apparent activation energy of 32 kJ mol^{-1} was well within the range of reported values for Cu,^[23] but higher than for Au-, Pt-, or Ru-based catalysts (Figure S7, Supporting Information).^[11] For better comparison with previously reported Cu catalysts, CuCl_{SA}/AC was evaluated under industrially relevant catalytic conditions for non-precious metals^[16] for 100 h ($T = 473 \text{ K}$, $\text{GHSV}(\text{C}_2\text{H}_2) = 70 \text{ h}^{-1}$, $\text{HCl}:\text{C}_2\text{H}_2 = 1.2$). Although the catalytic activity of CuCl_{SA}/AC was moderate compared to Au and Pt SACs, its stability on stream was remarkably high with an initial activity decay ($0.1\% \text{ h}^{-1}$) approximately ten times lower than state-of-the-art PGM catalysts.^[13] Consequently, coke deposition was found to be negligible over the 100 h run ($<1 \text{ wt}\%$, Figure S8 and Table S6, Supporting Information) and coke-related signals were absent in CW-EPR (see below). Compared to previously reported Cu acetylene hydrochlorination catalysts, CuCl_{SA}/AC was among the most stable, which can be partly ascribed to the absence of Cu nanoparticles or the lack of heteroatom dopants in the carbon carrier that may promote sintering or coke formation, respectively (Figure 1).^[28] The evaluation of catalysts prepared following the same procedure as CuCl_{SA}/AC but with increased metal content identified an optimal STY with 1 wt% Cu, which coincided with the maximum amount of sin-

gle atoms that could be stabilized before forming aggregates (Figure S9, Supporting Information). This observation mirrors the metal utilization in previously reported catalysts^[5] with high Cu contents (up to 25 wt%) not significantly improving catalyst activity (Figure S8, Supporting Information). The comparably high STY obtained for CuCl_{SA}/AC (Table S1, Supporting Information) suggests that extended copper phases (particularly CuCl_x) are likely spectator species in acetylene hydrochlorination and that isolated atoms represent the active entity of the metal.

2.2. Reaction-Induced Formation of Active Sites

The detailed ex situ analysis of as-prepared and used copper catalysts suggested that the convergence in the catalytic performance was caused by the reaction-induced transformation of the Cu nanoparticles into chlorinated single atom species (Figures S1–S4, Supporting Information). Although well known for ruthenium catalysts,^[12,29] the effect of acetylene hydrochlorination conditions on the redispersion of copper nanoparticles is not well established, with contradicting reports on nanoparticle size decreasing,^[30] remaining constant,^[17] or increasing^[31] upon use. Given the evidence for single atom active species, this would represent a unique case, wherein active sites self-form. To gain better insight into the dynamics of the formation of active and stable copper species, we sought to characterize CuCl_{SA}/AC and Cu_{NP}/AC under operando conditions.

To this end, CuCl_{SA}/AC and Cu_{NP}/AC were subjected to operando XAS tests. During the temperature ramping and catalyst drying step in helium the CuCl_{SA}/AC sample underwent autoreduction, which reflected in a drastic change in the XANES spectrum from Cu(II)- to Cu(I)-like, with a characteristic pre-edge feature (Figure 3a).^[32] The Cu_{NP}/AC catalyst that started as Cu(0) remained largely unmodified during the drying step in helium. Conversely, when exposed to the reaction mixture, the Cu_{NP}/AC sample slowly evolved a pre-edge feature as present in CuCl_{SA}/AC, which remained virtually unchanged in the latter catalyst. The effluents of the reactor were analyzed through mass spectrometry and revealed that both catalysts formed VCM when exposed to the reaction mixture (Figure 3b,c). The EXAFS spectrum of CuCl_{SA}/AC under reaction conditions was similar to the catalyst after drying in helium and remained virtually unaltered over time (Figure 3d). The coordination numbers derived from EXAFS spectral fittings at selected points in time (Figures S10 and S11 and Tables S7 and S8, Supporting Information), corroborated that the Cu SAC changed most extensively during drying in helium, while when exposed to the reaction mixture the coordination to Cl and O remained largely constant (Figure 3e). Interestingly, the Cu_{NP}/AC catalyst exhibited a decrease in Cu–Cu path intensity (expressed as $\text{CN}_{\text{Cu–Cu}}$) with a concurrent increase in a feature assigned to scattering with Cl or O (Figure 3f).

The abovementioned trends were readily captured when conducting XAS analysis under quasi in situ conditions, wherein the catalyst samples were isolated and transferred using standard air-free techniques (Figures S12 and S13, Supporting Information). Notably, the redispersion in quasi in situ experiments was more extensive as evidenced by the disappearance of Cu–Cu scattering, likely due to the higher reactant concentration in the laboratory reactor. In accordance with operando XANES, the quasi in

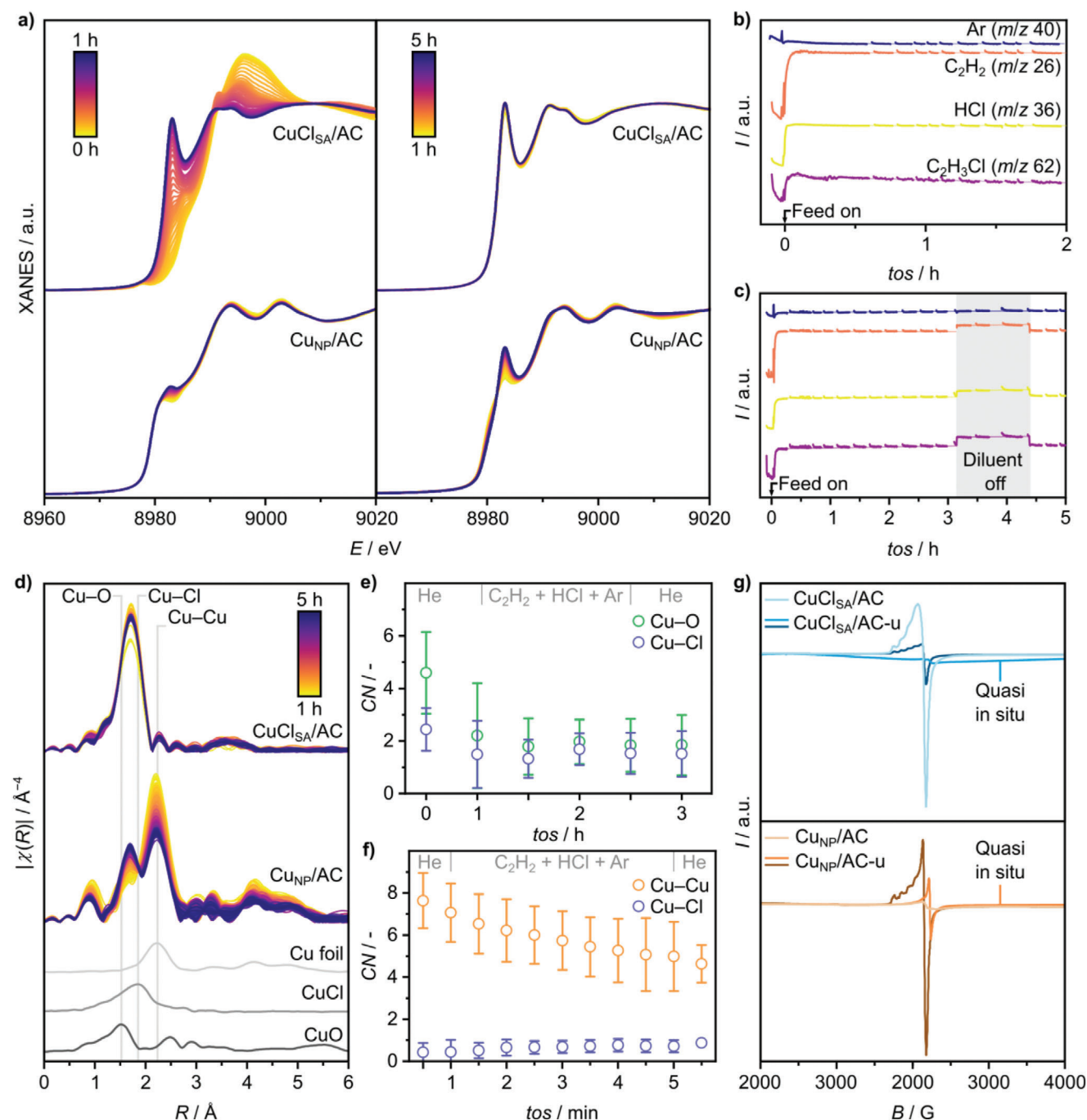


Figure 3. a) Operando Cu K-edge XANES spectra of the Cu-based catalysts during the heating ramp (left) and under reaction conditions (right) with time on stream (tos). Conditions left: $W_{\text{cat}} = 0.013$ g, heating rate 5 K min^{-1} , $T = 473 \text{ K}$, dwell time 30 min in He. Conditions right: $W_{\text{cat}} = 0.013$ g, $F_T = 65 \text{ cm}^3 \text{ min}^{-1}$, $T = 473 \text{ K}$, GHSV(C_2H_2) = 1200 h^{-1} , $\text{HCl}:\text{C}_2\text{H}_2 = 1:1$. b,c) Online mass spectrometry signals of acetylene hydrochlorination reactants and products with tos for CuCl_{SA}/AC (b) and CuNP/AC (c). The color code in (b) also applies to (c). d) Fourier-transformed EXAFS spectra of Cu-based catalysts under reaction conditions corresponding to the spectra in the right panel of (a). Regions of Cu–O, Cu–Cl, and Cu–Cu are highlighted with gray lines and reference spectra are shown underneath. e,f) EXAFS-derived coordination numbers (CN) for CuCl_{SA}/AC (e) and CuNP/AC (f) (detailed parameters indicated in Tables S7 and S8, Supporting Information). The gas compositions shown in inset refer to the values indicated above, except for measurements in helium, which were conducted at 303 K. g) Ex situ CW-EPR spectra (quasi in situ where indicated, see Figure S5, Supporting Information, for detailed fitting) of the Cu-based catalysts.

situ CW-EPR spectrum of $\text{CuCl}_{\text{SA}}/\text{AC-u}$ confirmed the absence of isolated Cu(II) , while Cu(I) is invisible to the technique; the observed spectral features were attributed to magnetically isolated and dipole-coupled Cu(0) centers (Figure 3g). Remarkably, quasi in situ spectra of $\text{Cu}_{\text{NP}}/\text{AC-u}$ displayed no contributions assigned to nanoparticles while a prominent signal ($g = 2.003$) corresponding to carbon-centered radicals present in carbonaceous deposits appeared.^[33] The absence of this signal in the CW-EPR spectrum of $\text{CuCl}_{\text{SA}}/\text{AC-u}$ together with the results of thermogravimetric analysis (TGA, Figure S9, Supporting Information) and sorption measurements (Table S6, Supporting Information) evidenced the resistance of the catalyst toward coke-forming reactions, supporting the stability of the atomically disperse architecture in acetylene hydrochlorination. Notably, the convergence in the EXAFS and CW-EPR spectra of $\text{Cu}_{\text{NP}}/\text{AC-u}$ and $\text{CuCl}_{\text{SA}}/\text{AC-u}$ underpinned the transformation of the distinct initial copper architectures (nanoparticles and isolated atoms) into a common structural motif.

The observations derived from operando and quasi in situ techniques revealed that considerable challenges arise in accurately characterizing the atomic-level structure of Cu active species in reported catalysts due to: (i) the complex nanoscale speciation of the employed catalytic materials and (ii) a lack of in situ characterization of the catalysts (Table S1, Supporting Information). Previously, the activity of Cu-based catalyst was attributed to Cu(II) ,^[23,34] or mixed-valence Cu(I)/Cu(II) sites^[17,31,35] based on the correlation of higher abundance of cationic Cu in the as-prepared and used catalysts (ex situ analysis) with improved catalytic activity. Such assignment can have consequences in theoretically derived reaction profiles that assume the CuCl_2 structure of the precursor is retained in the working catalyst.^[23] Our results confirmed that the assignment of oxidation states based on ex situ XPS and XAS measurements is not representative. Additionally, operando XAS analysis showed definitive proof of the formation of Cu(I)Cl species during reaction from the atomically isolated and nanoparticle initial architectures. Further, we show that the insights derived from operando analysis were paralleled by the more accessible quasi in situ conditions, demonstrating that the latter can also provide illustrative insights. Despite recent efforts to control metal nanostructure,^[23,36] the qualitative assessment of size effects in prior work concludes that the aggregation of Cu(II)/Cu(I) to Cu(0) nanoparticles is detrimental to catalyst activity,^[17,18] but the reaction-induced redispersion of Cu(0) was not considered. One reason for the preclusion of structural dynamics in previous work might be the high copper contents employed, which are likely to lead to full saturation of the anchoring sites and potentially mask redispersion processes that would occur otherwise. As a consequence of the high copper contents, metal nanoparticles were reported to grow.^[31] The nanoparticle redispersion observed herein supports the use of more simplistic catalyst compositions to address the dynamism at a fundamental level.

2.3. Molecular-Level Insights into the Restructuring and Reactivity

Aiming to obtain insights into the formation and stability of single atom species as the relevant active entity of the metal,

DFT simulations were conducted. Despite growing understanding of the importance of coordination site structures and their uniformity in SAC carriers, previous studies on Cu-based catalysts have not considered the interaction of the metal species with carbon supports.^[23,30] Here, we considered the diverse structures of oxygen-containing anchoring sites known to exist in activated carbons when constructing the structural models (Figure S14, Supporting Information).^[14,26] The local environment of the anchored metal atoms was investigated by simulating the adsorption and dechlorination of CuCl_2 at 473 K (Figures S15 and S16 and Table S9, Supporting Information). Over most defects, the mono- (CuCl) and dichlorinated (CuCl_2) metal sites were the energetically preferred structures with small differences (0.3 eV) in the free enthalpy of formation, G_{form} . The subsequent step to either ligand-free Cu or dimeric Cu_2Cl_2 species was endergonic (in the range of 0.2–2.0 eV with respect to CuCl) over most of the sites, except for tetraketonic defects (keto_4). Besides, these simulations could be represented in terms of the stability (quantified with E_{stab}) of the distinct single atom species compared against the bulk cohesive energy, that is, the driving force for aggregation (Figure 4a and Table S10, Supporting Information). Accordingly, the bulk cohesive energy superseded single atom stabilization for Cu_2Cl_2 and Cu for most oxygen anchoring sites, revealing that these structures were difficult to generate and inferior in terms of stability. For CuCl_2 and CuCl instead, dispersed atoms were thermodynamically preferred, indicating a clear tendency for Cu stabilization as chlorinated atoms (CuCl or CuCl_2) over most defects. The stability trends reflected in the Bader charge analysis (Table S9, Supporting Information) and core-level shifts (CLS, Figure S16, Supporting Information) were derived from the structural models. Experimental evidence of the $\text{CuCl}_{\text{SA}}/\text{AC}$ catalyst obtained from operando EXAFS spectra supported the presence of both CuCl and CuCl_2 (Figure 3b and Figure S12, Supporting Information), and ex situ CW-EPR pointed to epo_2^- and keto_4 -like geometries (Figure S5 and Table S5, Supporting Information), thus confining the set of relevant structure models further. On the basis of combined experimental and theoretical evidence, we focus our analysis on epo_2^- -bound, chlorinated copper atoms (CuCl/epo_2).

Considering the reaction-induced redispersion of Cu nanoparticles, and the distinct affinity of surface oxygen species on carbon toward chlorinated Cu atoms, we assessed the redispersibility of Cu nanoparticles by computing the disintegration Gibbs free energy, ΔG_{dis} , following the energetic formalism of Ouyang and co-workers.^[37] The calculation of ΔG_{dis} involves the average energetics of the aggregates of Cu (Cu_{NP}) or CuOCl (CuOCl_{NP} , Table S11, Supporting Information) and the formation energy of the single atom species (CuCl and CuCl_2) on each of the AC cavities (Figure S17, Supporting Information). The formation and stabilization of isolated CuCl_x superseded the energetic cost for breaking metal–metal bonds in a metallic Cu nanoparticle (Cu_{NP}) for all defects considered within (−1.7 to −0.2 eV, Figure 4b). Subsequent dechlorination into bare copper atoms was not favored (Figure 4c). When considering a redispersion route starting from oxychloride nanoparticles (CuOCl_{NP}), such as hypothesized for Ru,^[29] the stabilization of single atom species was endergonic in all cases (0.2–1.0 eV). Since CuOCl_{NP} is more stable, its disintegration is less likely than for the reduced phase (Table S12, Supporting Information); quasi in situ and operando XAS

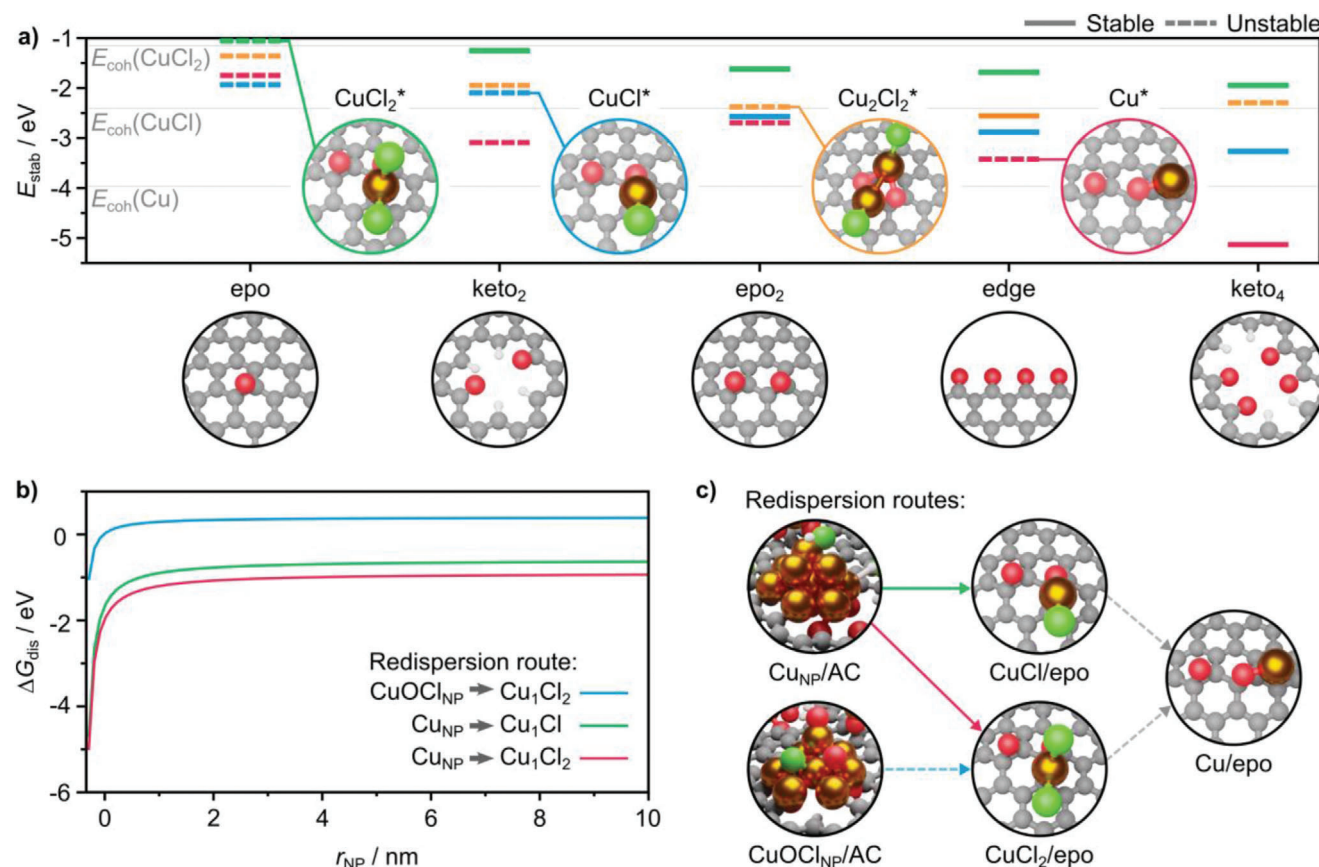


Figure 4. a) Stability of low nuclearity Cu_xCl_y ($x = 1-2$, $y = 0-2$, example structures shown in the inset) species anchored on oxygen-containing defects in the support (selected structures shown underneath) expressed in terms of the formation energy, E_{stab} . The dashed symbols represent regimes where the species are thermodynamically unstable, as quantified by the cohesive energy, E_{coh} . Defect codes: epo, monoepoxide; epo₂, diepoxide; keto₂, diketone; keto₄, tetraketone; edge, edge carbonyl (all structures are shown in Figure S10, Supporting Information). b) Free Gibbs enthalpy of disintegration, ΔG_{dis} , of Cu_{NP} and CuOCl_{NP} with different radius, r_{NP} , into single atom species anchored on epo₂ defects. c) Scheme of the disintegration routes represented in (b) (full details in Figure S13 and Table S9, Supporting Information). Color code for structures: C, gray; O, red; Cl, green; Cu, orange.

confirmed that the formation of metallic Cu preceded nanoparticle redispersion under reaction conditions.

To assess the activity of all possible metal sites in $\text{CuCl}_{\text{SA}}/\text{AC}$, we computed the adsorption energy of acetylene, $E_{\text{ads}}(\text{C}_2\text{H}_2)$, which was previously identified as an activity descriptor.^[11] This metric was closely related to the stability of the site structure as quantified by E_{stab} . For ligand-free Cu single atoms, Cu/epo_2 had the most favorable combination of $E_{\text{ads}}(\text{C}_2\text{H}_2)$ and high E_{stab} (Figure 5a and Table S13, Supporting Information). Notably, all CuCl structures displayed narrowly distributed and more positive (i.e., less beneficial) values for $E_{\text{ads}}(\text{C}_2\text{H}_2)$ than for configurations with ligand-free Cu. Since the results suggest that a distinction between different CuCl structures is unlikely to affect site activity significantly and based on experimental evidence from ex situ CW-EPR and operando EXAFS spectroscopy, CuCl/epo_2 -b (bidentate configuration) was chosen as a stable and representative proxy of the active sites. The reaction profile over the identified active site (CuCl/epo_2 -b) involved the endergonic insertion of acetylene into the Cu–Cl bond first (R1 in Figure 5b and Figure S18 and Table S14, Supporting Information), driven by the subsequent activation of HCl releasing ≈ 0.2 eV (R2). The splitting of HCl occurred under the participation of the carbon

scaffold (intermediate $\text{C}_2\text{H}_2(\text{Cl})\text{--H--Cl}$) and preceded the rate-limiting proton transfer step (R3) before releasing $\text{C}_2\text{H}_3\text{Cl}$ and favorably regenerating CuCl (-0.9 eV). Except for minor differences, CuCl species followed previously reported mechanisms of acetylene hydrochlorination over precious-metal SACs.^[11,13] Combined DFT, in-depth characterization, and performance data indicates that the active site is composed of mononuclear Cu(I)Cl species stabilized on surface-oxygen functionalities, likely diepoxide defects, of the carbon support.

2.4. Life-Cycle Assessment of Acetylene Hydrochlorination Catalysts

Our results confirmed the structural origin of the unparalleled stability of carbon-supported copper SACs in acetylene hydrochlorination, but their productivity remains limited compared to precious metal-based alternatives. Thus, it is unclear whether the benefits of using earth-abundant metals will outweigh the use of carbon-intensive precious metals. LCA analysis bridges the molecular and process levels, providing a comprehensive picture of the environmental performance of catalytic systems based on

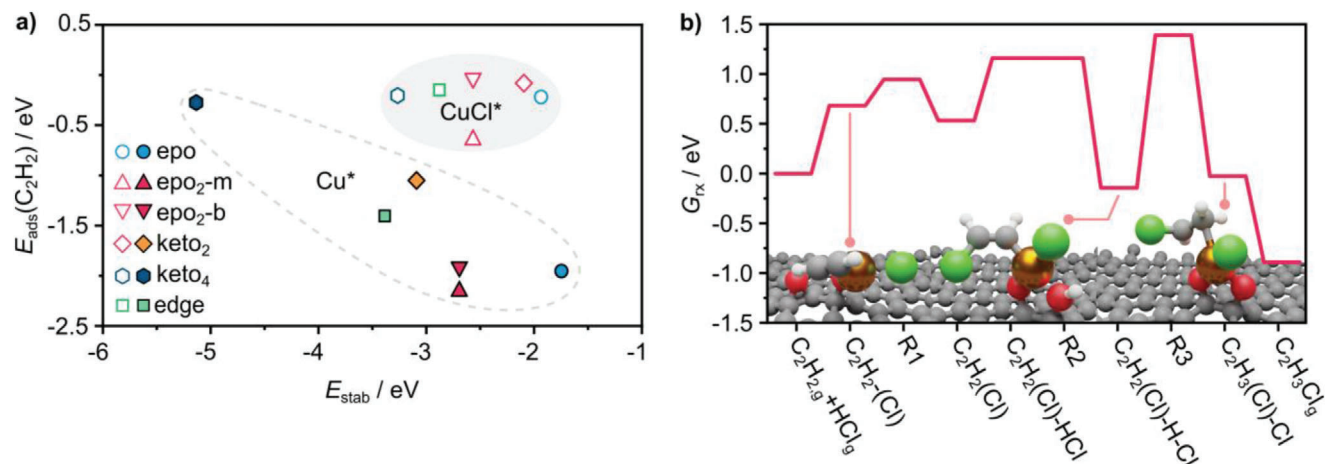


Figure 5. a) Acetylene adsorption energy, $E_{\text{ads}}(\text{C}_2\text{H}_2)$, as a function of SAC stability, E_{stab} . Mono- (-m) and bi- (-b) dentate anchoring configurations over the epo₂ defect were considered separately. b) Profile of the Gibbs free reaction enthalpy, G_{rx} , of acetylene hydrochlorination over a CuCl/epo₂ site, chosen as representative and stable configuration of the active site. Reactant configurations involved in key reaction steps are schematically shown inset (all steps in Figure S14, Supporting Information). Color code for structures: C, gray; O, red; Cl, green; Cu, orange.

their activity, stability, and the sourcing of their starting materials, helping to elucidate the extent to which novel technologies are greener.^[25,38] However, a comparison of acetylene hydrochlorination catalysts is lacking. To this end, we evaluated the impact of state-of-the-art acetylene hydrochlorination benchmarks (i.e., AuS/AC,^[2] Pt_{SA}/AC,^[13] and CuCl_{SA}/AC) with respect to the commercially applied HgCl₂/AC catalyst using LCA (parameters in Tables S15 and S16, Supporting Information). To address the multidimensionality of sustainability aspects, we evaluated the impact categories global warming potential (GWP), human health, ecosystems quality, and resource scarcity. We based our analysis on the carbon footprint associated with the catalytically active metal employed; a key determinant of catalyst footprint (Figure 6a).^[25] For example, the scarcity of gold and platinum results in a high GWP of 28 and 16 tons_{CO₂-eq} kg_{Au}⁻¹, respectively, while the low footprint of copper (9 kg_{CO₂-eq} kg_{Cu}⁻¹) bears potential for low-footprint acetylene hydrochlorination catalysts. Across all impact categories analyzed, the HgCl₂/AC catalyst revealed the largest footprint of all systems (Figure 6b), which was mainly caused by the loss of mercury through volatilization.^[2,14] In particular, volatile Hg emissions increased the impact on human health and ecosystems quality categories by two orders of magnitude compared to Pt_{SA}/AC and AuS/AC catalysts. Compared to HgCl₂/AC, the sustainability metrics of AuS/AC and Pt_{SA}/AC improved in all categories and were in the same order of magnitude for both metals. Catalysts based on these metals are environmentally beneficial because they achieve high VCM productivities (in kg_{VCM} kg_{cat}⁻¹, see Table S15, Supporting Information) and eliminate the issues associated with mercury volatilization. Still, the LCA-derived metrics of CuCl_{SA}/AC were almost two orders of magnitude lower than those of AuS/AC and Pt_{SA}/AC. Compared to other previously reported copper catalysts (Table S16, Supporting Information), CuCl_{SA}/AC displayed one of the lowest carbon footprints with a particularly low impact contribution of copper, demonstrating the relevance of our simplified modifier-free and low metal content approach to catalyst design (Figure S19, Supporting Information).

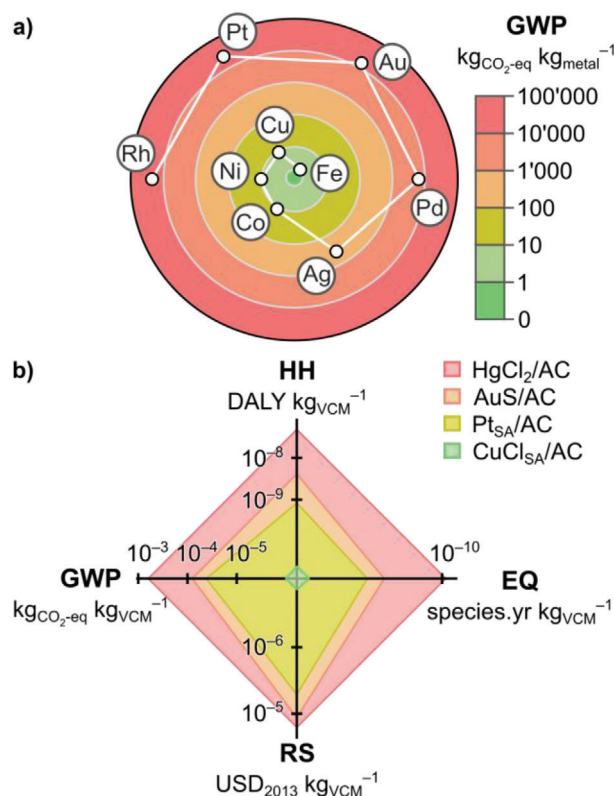


Figure 6. a) Carbon footprint associated with the sourcing of most relevant catalytic transition metals expressed in terms of global warming potential (GWP in kg of CO₂ equivalents).^[44] b) LCA-derived midpoints in GWP and endpoints in human health (HH in disability-adjusted life years, DALY), ecosystems quality (EQ in species years), and resource scarcity (RS in US dollars) for best-performing copper catalysts compared to state-of-the-art gold^[2] and platinum systems,^[11] and the commercially applied mercury chloride catalyst.^[2]

Researchers frequently choose catalytic systems offering maximal productivity as an essential step for implementing new processes. Although adapting catalyst synthesis may allow for the use of greener solvents^[15] and the selection and modification of the carbon support may improve catalyst longevity^[14] and anchoring site density,^[39] this study clearly shows the priority for sustainable VCM production stems from the choice of earth-abundant metals providing moderate but stable activity. The sustainability footprint of copper metal is extremely favored compared to mercury-based systems used in industry or precious metal-based alternatives extensively studied in the literature. This conclusion prompts a paradigm shift toward prioritizing sustainability metrics as the main driver in catalytic process design. Building on the fundamental understanding of Cu-catalyzed acetylene hydrochlorination, future efforts should focus on improving the efficiency of copper catalysts. Fortunately, previous work has shown the potential of diverse promotion strategies,^[23,40] which may hold promise if critically re-evaluated under close consideration of the dynamic evolution of optimized nanostructures and the environmental footprint.

3. Conclusions

We have explored the optimal nanostructure of carbon-supported copper species, which have recently emerged as stable catalysts for acetylene hydrochlorination by studying systems with controlled nuclearity and speciation. Detailed characterization revealed that independent of the initial catalyst architecture, reaction-induced restructuring led to the formation of atomically dispersed copper species coordinated to oxygen defects in the support, resulting in a convergence in the STY and similar stable performance. Importantly, operando techniques provided unambiguous evidence for the autoreduction of the SAC to Cu(I)Cl prior to the reaction, while copper nanoparticles underwent continuous evolution under reaction conditions. DFT calculations highlighted the stability of chlorinated single atoms of Cu across distinct anchoring sites that acted as a driving force for nanoparticle redispersion. The identity of the oxygen defect structure did not impact the acetylene adsorption energy and the key role of the support in stabilizing key intermediates (e.g., $C_2H_2(Cl)-H-Cl$) in the catalytic cycle. Using optimal metal contents and adapted reaction conditions, we demonstrated the potential for stable performance for over 100 h with one of the highest reported productivities for copper on a per-metal basis.

Although less active than state-of-the-art Au- or Pt-based systems, LCA-derived metrics indicated that Cu SACs have the potential to substantially improve the catalyst footprint in VCM production by up to two orders of magnitude, emphasizing the value of focusing on catalysts based on earth-abundant metals. Furthermore, our modifier-free, low metal content catalyst improves over the environmental impact of previously reported copper catalysts. Together with the sustainability analysis, the in-depth understanding of reaction-induced structural dynamics and active site formation mechanism represents an opportunity to revisit known modifiers and their interaction with atomically dispersed Cu for improved catalyst performance. In covering aspects from atomic-scale catalyst design to precise characterization and metrics-based process impact analysis, this work represents an

example of how catalyst engineering across scales could improve the sustainability of chemical manufacturing.

4. Experimental Section

Catalyst Synthesis: Activated carbon (AC, Norit Rox 0.8, Cabot Corp., 0.4–0.6 mm particle size) was purified by stirring in an aqueous nitric acid solution (1 M, 40 cm³ g_{AC}^{−1}, puriss., Sigma-Aldrich) for 30 min, followed by thorough washing with deionized water, and drying (338 K). For the synthesis of the chlorinated single-atom catalyst (SAC), CuCl_{SA}/AC, CuCl₂·2H₂O (99.99%, abcr) corresponding to a nominal content of 1 wt% was dissolved in ethanol (1.5 cm³ g_{AC}^{−1}, 99.8%, Sigma-Aldrich), deposited dropwise onto the purified AC, and dried overnight (338 K). Subsequently, the powder was annealed in a static N₂ atmosphere (473 K, 3 h hold, 5 K min^{−1} ramp). This standard procedure was adapted to obtain the chlorine-free SAC Cu_{SA}/AC by replacing CuCl₂·2H₂O with the appropriate amount of Cu(NO₃)₂·3H₂O (puriss., Sigma-Aldrich). To obtain a catalyst containing metallic nanoparticles (Cu_{NP}/AC) the annealing procedure was conducted in a tubular oven under nitrogen flow at an elevated temperature (873 K, 3 h hold, 5 K min^{−1} ramp). For reference purposes, catalysts with different nominal Cu content (0.5, 2, and 5 wt%) were prepared, following the same procedure for CuCl_{SA}/AC.

Catalyst Characterization: Powder X-ray diffractograms were acquired in a PANalytical X'Pert PRO-MPD instrument (Bragg–Brentano geometry) using a Ni-filtered Cu K α source. Data were collected at 2 θ in the range of 3–70° with a step size of 0.08° and a collection time of 162 s.

For electron microscopy, the catalyst samples were dusted onto standard carbon-film nickel grids (300 mesh). High-angle annular dark-field scanning transmission electron microscopy (HAADF-STEM) was performed on an FEI Talos F200X microscope (200 kV acceleration potential). Aberration-corrected HAADF-STEM images were acquired on a Hitachi HD-2700CS instrument operated at 200 kV. Image frames of 1024 × 1024 px were acquired with 15 μ s dwell time.

XPS was conducted on a Physical Electronics Instruments Quantum 2000 instrument with monochromatic Al K α radiation (15 kV, 32.3 W). Due to instrumental limitations, sample introduction required intermediate exposure to air, which was known to cause oxidation of copper.^[41] The spectral acquisition occurred under ultrahigh vacuum conditions (5 × 10^{−8} Pa residual pressure) with a pass energy of 46.95 eV. All XPS signals were referenced using the aliphatic peak in the C 1s photoemission which was set at 284.8 eV. Due to a lack of suited reference materials and the low representativity of ex situ analyses, data analysis was conducted using a simplified estimation of the Auger parameter. To this end, the Auger parameters of the calibrated spectra were determined manually according to the standard procedure using the CasaXPS software.^[42]

XAS measurements were conducted at the X10DA (SuperXAS) beamline of the Swiss Light Source.^[43] The X-ray beam from the 2.9 T super-bend was collimated using a Si-coated mirror at 2.9 mrad, monochromatized using a liquid nitrogen cooled Si(111) channel-cut monochromator, and focused to a spot size of 1000 × 200 μ m (horizontal × vertical) using a Rh-coated toroidal double focusing mirror. Quick XAS data were measured using 1 Hz monochromator oscillations for 2 min and averaged. X-ray damage was checked on a 5 s time scale and excluded. Data were acquired from pressed pellets at the Cu K-edge in transmission mode, using three 15 cm long N₂-filled ionization chambers. Additional samples were prepared under the exclusion of air to allow for a quasi in situ investigation of the catalysts. To this end, catalysts samples before (dried at 473 K, 3 h in flowing He) and after catalytic tests (10 h under standard conditions, see below) were transferred into quartz glass capillaries (1 mm outer diameter, 0.01 mm wall thickness, 80 mm length, Hilgenberg GmbH) and sealed in an inert atmosphere. The samples were placed between the first and the second ionization chamber and measured in fluorescence mode using a passivated implanted planar silicon diode detector.^[44] Transmission geometry configuration was used for the analysis under operando conditions, wherein a dilute reaction mixture ($F_T = 65$ cm³ STP min^{−1}, 0.91 vol% C₂H₂, 1 vol% HCl, rest Ar) was fed into a quartz capillary filled

with the catalyst sample ($W_{\text{cat}} = 13$ mg) at atmospheric pressure. The catalyst was heated using two heating cartridges placed above and below the capillary and controlled with a thermocouple placed in the middle of the catalyst bed. Gaseous effluents were analyzed using a mass spectrometer (Pfeiffer Vacuum ThermoStar GSD T1); due to the corrosive nature of the reactants the mass spectrometry scans were intermittently stopped. For the absolute energy calibration, a metallic Cu foil was measured simultaneously between the second and third ionization chambers. The resulting spectra were energy calibrated, background corrected, and normalized using ProQEXAFS software^[45] available at SuperXAS and the Athena program from the Demeter software suite.^[46] The XANES of the ex situ samples was analyzed through linear combination fitting of the sample spectra with reference compounds using the Athena program (Table S2, Supporting Information). EXAFS spectral fitting was performed using the Artemis program applying the parameters described in Table S4, Supporting Information.^[46]

CW-EPR spectroscopy experiments were performed on a Bruker Elexsys E500 spectrometer equipped with an Oxford helium (ESR900) cryostat operating at X-band frequencies (9.4 GHz) using a ER4122SHQE Bruker EPR Resonator. CW-EPR spectra were acquired at 40 K and a microwave power of 2.002 mW (power attenuation 20 dB). For detection, a magnetic field modulation of 0.3 mT and 100 kHz was applied, and the modulated signal was amplified by a lock-in amplifier (conversion time 655.36 ms, time constant 163.84 ms), sweeping the magnetic field with a center field 300 mT and sweep width of 590 mT. All measured g factors were offset-corrected against a known standard (i.e., free radical 1,1-diphenyl-2-picrylhydrazyl). The spectra were simulated using the Easyspin package.

TGA was carried out in a Linseis STA PT 1600 instrument using an alumina crucible. The sample (≈ 20 mg) was dried (373 K, 1 h) and subsequently heated to 1273 K (heating ramp 10 K min⁻¹) in a dilute oxygen atmosphere (300 cm³ min⁻¹, 6.6 vol% O₂ in Ar). On-line effluent analysis of gaseous products (CO and CO₂) was conducted using a mass spectrometer (Pfeiffer Vacuum ThermoStar GSD T1).

Argon sorption was performed on a Micromeritics 3Flex analyzer. Catalyst samples were degassed for 10 h at 473 K (0.1 mbar) before being subjected to analysis at 77 K.

Catalyst Evaluation: The hydrochlorination of acetylene was studied at atmospheric pressure in a continuous-flow fixed-bed microreactor reported elsewhere.^[11,13,14] In short, the gases C₂H₂ (PanGas, purity 2.6), HCl (Air Liquide, purity 2.8, anhydrous), Ar (PanGas, purity 5.0, internal standard), and He (PanGas, purity 5.0) were mixed into a gas feed using mass-flow controllers. The catalyst ($W_{\text{cat}} = 0.2$ g) was suspended between quartz wool pads in a tubular quartz reactor (10 mm inner diameter) and placed in an electrical oven. The temperature was controlled by a thermocouple located in a quartz thermowell with the tip positioned in the center of the catalyst bed. First, the catalyst was heated in flowing He ($T = 473$ K, 30 min, ≈ 10 K min⁻¹) before exposure to the reaction mixture ($F_T = 15$ cm³ STP min⁻¹, 40 vol% C₂H₂, 44 vol% HCl, and 16 vol% Ar, GHSV(C₂H₂) = 670 h⁻¹). Stability tests (100 h) were conducted under industrially relevant conditions ($W_{\text{cat}} = 1.2$ g, $F_T = 10$ cm³ STP min⁻¹, 38 vol% C₂H₂, 46 vol% HCl, 16 vol% Ar, GHSV(C₂H₂) = 70 h⁻¹, $T = 473$ K). Carbon-containing compounds (C₂H₂ and C₂H₃Cl) and Ar were quantified on-line via a gas chromatograph equipped with a GS-Carbon PLOT column coupled to a mass spectrometer (Agilent, GC 7890B, Agilent MSD 5977 A). Since VCM was the only product detected in all the tests, the catalytic activity was presented as the yield of VCM (Y) calculated according to Equation (1), where $n_{\text{out}}(\text{VCM})$ and $n_{\text{in}}(\text{C}_2\text{H}_2)$ represented the respective molar flows of VCM and C₂H₂ at the reactor outlet and inlet.

$$Y = \frac{n_{\text{out}}(\text{VCM})}{n_{\text{in}}(\text{C}_2\text{H}_2)} \times 100\% \quad (1)$$

The STY of VCM was determined with Equation (2) with $M(\text{VCM})$ the molar mass of VCM and $w_B(\text{Cu})$ the bulk Cu content (in wt%).

$$\text{STY} = \frac{n_{\text{out}}(\text{VCM})}{W_{\text{cat}} \times w_B(\text{Cu})} \times M(\text{VCM}) \quad (2)$$

The error of the carbon balance ϵ , determined using Equation (3),

$$\epsilon = \frac{n_{\text{in}}(\text{C}_2\text{H}_2) - n_{\text{out}}(\text{VCM}) - n_{\text{out}}(\text{C}_2\text{H}_2)}{n_{\text{in}}(\text{C}_2\text{H}_2)} \times 100 \quad (3)$$

was less than 5% in all experiments. After the tests, the reactor was quenched to room temperature in He flow and the catalytic materials were retrieved for further characterization.

Computational Methods: All DFT calculations were performed using the Vienna Ab initio Simulation Package (VASP).^[47,48] The generalized gradient approximation of the Perdew–Burke–Ernzerhof functional^[49] was used to obtain the exchange-correlation energies with dispersion contributions introduced via Grimme's DFT-D3 approach.^[50] Projector augmented wave^[51,52] and plane waves with a cut-off energy of 450 eV, with spin polarization allowed when needed, were chosen to represent the inner electrons and the valence mono-electronic states, respectively. A vacuum region between slabs of at least 12 Å and a dipole correction along the z -axis were employed for all slab models.^[53] For all investigated systems, structures were relaxed using convergence criteria of 10⁻⁴ and 10⁻⁵ eV for the ionic and electronic steps, respectively.

The structural parameters (Table S5, Supporting Information) for the analysis of experimental CW-EPR spectra were determined with Kohn–Sham DFT, using a B3LYP functional with a spin-unrestricted shell and a DGTZVP basis set in the Gaussian and Orca software.

To describe the extensive phase space of chemical environments in AC,^[13] a set of five cavities was constructed for the simulation of the AC support, comprising slabs (6 × 6) of graphitic carbon with mono- to tetra-coordinated configurations with epoxide and carbonyl functionalities: (i) monoepoxide (epo), (ii) diepoxide (epo₂), (iii) di-ketone (keto₂), (iv) tetraketone (keto₄), and (v) edge carbonyl (edge) cavities (Figure S14, Supporting Information).

Single-atom catalysts were modeled by placing CuCl _{x} ($x = 0–2$) moieties at the center of the distinct AC cavities, with subsequent removal of chlorine to the gas-phase reservoir, and the Bader charges and CLS (Table S9, Supporting Information) of the resulting species were calculated. Entropic contributions from Cl₂ were considered. Gas-phase molecules were optimized in a box of 15.0 × 15.5 × 16.0 Å³.

To model nanoparticle disintegration, the energetic formalism of Ouyang and co-workers was adapted.^[37] The feasibility of the process could be described by the Gibbs free energy of disintegration, ΔG_{dis} , as quantified with Equation (4)

$$\Delta G_{\text{dis}}(r_{\text{NP}}, T, P) = E_{\text{stab}} - x\Delta\mu_{\text{HCl}}(T, P) - \Delta E_{\text{NP}}(r_{\text{NP}}) \quad (4)$$

wherein the energy of removing a Cu atom from a nanoparticle with radius r_{NP} is expressed as $\Delta E_{\text{NP}}(r_{\text{NP}})$ and balanced with the formation energy of adsorbed CuCl _{x} ($x = 1–2$) species (quantified by E_{stab} , Table S10, Supporting Information) and a chemical potential term, $\Delta\mu(T, P)$ (−0.34 eV at 473 K and 0.44 bar HCl). Configurational entropic contributions were not included in the model due to the difficulty in assessing the precise composition and distribution of sites in AC. The Gibbs free energy of disintegration was calculated both for Cu and CuClO nanoparticles, to account for the potential oxychlorination of Cu phases under reaction conditions. Three different routes for disintegration were considered, corresponding to the formation CuCl and CuCl₂ (Table S9, Supporting Information).

The value of $\Delta E_{\text{NP}}(r_{\text{NP}})$ was computed with Equation (5) for structures of Cu and CuClO, where Ω corresponds to the molar volume of the bulk structure, f_i to the ratio of exposed facets, γ_i to the surface energies of the respective facets, and θ_{HCl} to the surface coverage with HCl (Table S8, Supporting Information).

$$\Delta E_{\text{NP}}(r) = \frac{3\Omega \cdot \sum_i f_i \gamma_i (\theta_{\text{HCl}})}{R} \quad (5)$$

The molar volume was found to be 11.36 Å atom⁻¹ for Cu and 54.10 Å per formula unit of CuClO. To model Cu nanoparticles, (4 × 4) slabs of three low-Miller-index planes, (111), (110), and (100) were simulated. The

(111) and (100) facets were modeled with four atomic layers, and the (110) facet was constructed with eight atomic layers. The (001) facet of the orthorhombic oxychlorinated phase of Cu (CuClO) was modeled with two layers of CuClO. The crystal morphology model for the Wulff construction was created using VESTA (v4.5.0). The shapes were described as a function of surface energies and the symmetry point group of the nanoparticle.

In all nanoparticle models, the half-bottom layers were kept fixed to the bulk configuration, while the half-upper ones were fully relaxed. The interaction of the metal particles with HCl was only considered for Cu phases at two different coverages ($\theta_{\text{HCl}} = 0.125\text{--}0.5\text{ ML}$), as it was assumed that the surface energy of CuClO, where the Cu atoms were fully coordinated, would not experience significant differences when considering the interaction with HCl. Surface interactions with C_2H_2 did not result in mobile Cu fragments and hence were not considered here.

The Brillouin zone for all models was sampled through a gamma-centered grid of $3 \times 3 \times 1$ of k -points except for CuClO, where a gamma-centered grid of $2 \times 2 \times 1$ k -points was employed instead. All the structures presented in this work were uploaded to the ioChem-BD database.^[54,55]

Life-Cycle Assessment: The environmental impact of each type of catalyst was determined via LCA following the ISO 14040/44 framework with the functional unit being the amount of catalyst required to produce 1 kg of VCM ($\text{kg}_{\text{VCM}}^{-1}$). The life-cycle inventory calculations were implemented in SimaPro (v.9.2.0.2), combining data from the foreground (catalyst) and background systems (all the activities connected to the foreground), which include feedstock, emissions, and waste associated with the catalyst, under the assumption that the metal contained in the catalyst was the main contributor toward its total impact. In the case of the HgCl_2/AC catalyst, the Hg emissions associated with catalyst use were also considered.^[4] The background data were retrieved from Ecoinvent (v3.5), using the allocation at the point of substitution system model version of the database, based on an attributional approach and selecting the global markets for the metals.^[56] The impact of phosphorus- and nitrogen-containing modifiers was approximated through the use of data for phosphorus trichloride and N,N -dimethyl formamide, as representative proxies. The required quantity of catalyst (foreground system) was calculated based on literature and experimental data (Tables S15 and S16, Supporting Information). The background system included all upstream activities related to producing the active metal contained in the catalyst. Finally, the life cycle impact assessment phase was carried out following the ReCiPe 2016 method (v1.03) implemented in SimaPro.^[57]

Statistical Analysis: The relative error for all catalytic tests was controlled through three independent measurements. Because the standard deviation was below the size of the employed symbols, error bars were omitted to improve visibility. Unless otherwise specified in the methods section, the displayed characterization data represented raw data based on one measurement. The use of proprietary software packages for dedicated data analysis was indicated where used and fitted parameters (e.g., for XANES and EXAFS) were reported together with the relevant metric for uncertainty. All fittings were made available together with the raw data.

Supporting Information

Supporting Information is available from the Wiley Online Library or from the author.

Acknowledgements

This publication was created as part of NCCR Catalysis (grant number 180544), a National Centre of Competence in Research funded by the Swiss National Science Foundation. ScopeM at ETH Zurich is acknowledged for access to their facilities. A.R.-F. acknowledges funding from the Generalitat de Catalunya and the European Union (Grant 2021FI_B 00109). The Spanish Ministry of Science and Innovation is acknowledged for financial support (PID2021-122516OB-I00 and Severo Ochoa Grant MCIN/AEI/10.13039/501100011033 CEX2019-

000925-S) and the Barcelona Supercomputing Center–Spanish Supercomputing Network (BSC-RES) for providing generous computing resources. V. Giulimondi, I. Surin, P.O. Willi and R.N. Grass are thanked for assistance with sample preparation and quasi in situ and operando measurements.

Open access funding provided by Eidgenössische Technische Hochschule Zurich.

Conflict of Interest

The authors declare no conflict of interest.

Data Availability Statement

The data that support the findings of this study are openly available in Zenodo at <https://doi.org/10.5281/zenodo.7380519>, reference number 7380519.

Keywords

acetylene hydrochlorination, copper speciation, life-cycle assessment, reaction-induced restructuring, single-atom catalysis

Received: December 7, 2022

Revised: March 2, 2023

Published online: May 12, 2023

- [1] R. Lin, A. P. Amrute, J. Pérez-Ramírez, *Chem. Rev.* **2017**, *117*, 4182.
- [2] P. Johnston, N. Carthey, G. J. Hutchings, *J. Am. Chem. Soc.* **2015**, *137*, 14548.
- [3] I. T. Trots, T. Zimmermann, F. Schüth, *Chem. Rev.* **2014**, *114*, 1761.
- [4] G. Zichittella, A. Ceruti, G. Guillén-Gosálbez, J. Pérez-Ramírez, *Chem* **2022**, *8*, 883.
- [5] D. M. Smith, P. M. Walsh, T. L. Slager, *J. Catal.* **1968**, *11*, 113.
- [6] G. Hutchings, *J. Catal.* **1985**, *96*, 292.
- [7] G. Malta, S. A. Kondrat, S. J. Freakley, C. J. Davies, L. Lu, S. Dawson, A. Theftford, E. K. Gibson, D. J. Morgan, W. Jones, P. P. Wells, P. Johnston, C. R. A. Catlow, C. J. Kiely, G. J. Hutchings, *Science* **2017**, *355*, 1399.
- [8] S. K. Kaiser, R. Lin, S. Mitchell, E. Fako, F. Krumeich, R. Hauert, O. V. Safonova, V. A. Kondratenko, E. V. Kondratenko, S. M. Collins, P. A. Midgley, N. López, J. Pérez-Ramírez, *Chem. Sci.* **2019**, *10*, 359.
- [9] S. K. Kaiser, Z. Chen, D. F. Akl, S. Mitchell, J. Pérez-Ramírez, *Chem. Rev.* **2020**, *120*, 11703.
- [10] S. Ding, M. J. Hülsey, J. Pérez-Ramírez, N. Yan, *Joule* **2019**, *3*, 2897.
- [11] S. K. Kaiser, E. Fako, I. Surin, F. Krumeich, V. A. Kondratenko, E. V. Kondratenko, A. H. Clark, N. López, J. Pérez-Ramírez, *Nat. Nanotechnol.* **2022**, *17*, 606.
- [12] S. K. Kaiser, R. Lin, F. Krumeich, O. V. Safonova, J. Pérez-Ramírez, *Angew. Chem., Int. Ed.* **2019**, *58*, 12297.
- [13] S. K. Kaiser, E. Fako, G. Manzocchi, F. Krumeich, R. Hauert, A. H. Clark, O. V. Safonova, N. López, J. Pérez-Ramírez, *Nat. Catal.* **2020**, *3*, 376.
- [14] S. K. Kaiser, I. Surin, A. Amorós-Pérez, S. Büchele, F. Krumeich, A. H. Clark, M. C. Román-Martínez, M. A. Lillo-Ródenas, J. Pérez-Ramírez, *Nat. Commun.* **2021**, *12*, 4016.
- [15] S. K. Kaiser, A. H. Clark, L. Cartocci, F. Krumeich, J. Pérez-Ramírez, *Small* **2021**, *17*, 2004599.
- [16] H. Xu, G. Luo, *J. Ind. Eng. Chem.* **2018**, *65*, 13.
- [17] X. Wang, M. Zhu, B. Dai, *ACS Sustainable Chem. Eng.* **2019**, *7*, 6170.
- [18] Y. Zhai, J. Zhao, X. Di, S. Di, B. Wang, Y. Yue, G. Sheng, H. Lai, L. Guo, H. Wang, X. Li, *Catal. Sci. Technol.* **2018**, *8*, 2901.

- [19] Y. Ren, B. Wu, F. Wang, H. Li, G. Lv, M. Sun, X. Zhang, *Catal. Sci. Technol.* **2019**, 9, 2868.
- [20] B. B. Sarma, F. Maurer, D. E. Doronkin, J.-D. Grunwaldt, *Chem. Rev.* **2023**, 123, 379.
- [21] X. Li, X. Yang, J. Zhang, Y. Huang, B. Liu, *ACS Catal.* **2019**, 9, 2521.
- [22] E. D. Boyes, A. P. LaGrow, M. R. Ward, R. W. Mitchell, P. L. Gai, *Acc. Chem. Res.* **2020**, 53, 390.
- [23] T. Wang, Z. Jiang, Q. Tang, B. Wang, S. Wang, M. Yu, R. Chang, Y. Yue, J. Zhao, X. Li, *Commun. Chem.* **2022**, 5, 2.
- [24] B. Wang, T. Zhang, Y. Liu, W. Li, H. Zhang, J. Zhang, *Appl. Catal. Gen. A* **2022**, 630, 118461.
- [25] D. F. Akl, D. Poier, S. C. D'Angelo, T. P. Araújo, V. Tulus, O. V. Safonova, S. Mitchell, R. Marti, G. Guillén-Gosálbez, J. Pérez-Ramírez, *Green Chem.* **2022**, 24, 6879.
- [26] S. Büchele, G. Zichittella, S. Kanatakis, S. Mitchell, J. Pérez-Ramírez, *ChemCatChem* **2021**, 13, 2599.
- [27] E. Vorobyeva, V. C. Gerken, S. Mitchell, A. Sabadell-Rendón, R. Hauert, S. Xi, A. Borgna, D. Klose, S. M. Collins, P. A. Midgley, D. M. Kepaptsoglou, Q. M. Ramasse, A. Ruiz-Ferrando, E. Fako, M. A. Ortuño, N. López, E. M. Carreira, J. Pérez-Ramírez, *ACS Catal.* **2020**, 10, 11069.
- [28] R. Lin, S. K. Kaiser, R. Hauert, J. Pérez-Ramírez, *ACS Catal.* **2018**, 8, 1114.
- [29] V. Giulimondi, S. K. Kaiser, M. Agrachev, F. Krumeich, A. H. Clark, S. Mitchell, G. Jeschke, J. Pérez-Ramírez, *J. Mater. Chem. A* **2021**, 10, 5953.
- [30] B. Wang, T. Zhang, Y. Liu, W. Li, H. Zhang, J. Zhang, *Appl. Catal. A* **2022**, 630, 118461.
- [31] Y. Han, Y. Wang, Y. Wang, Y. Hu, Y. Nian, W. Li, J. Zhang, *Appl. Organomet. Chem.* **2021**, 35, e6066.
- [32] F. Amano, T. Tanaka, T. Funabiki, *J. Mol. Chem* **2004**, 221, 89.
- [33] A. Cesarini, S. Mitchell, G. Zichittella, M. Agrachev, S. P. Schmid, G. Jeschke, Z. Pan, A. Bodi, P. Hemberger, J. Pérez-Ramírez, *Nat. Catal.* **2022**, 5, 605.
- [34] C. Zhao, X. Zhang, Z. He, Q. Guan, W. Li, *Inorg. Chem. Front.* **2020**, 7, 3204.
- [35] K. Zhou, J. Si, J. Jia, J. Huang, J. Zhou, G. Luo, F. Wei, *RSC Adv.* **2014**, 4, 7766.
- [36] B. Wang, Z. Jiang, T. Wang, W. Tang, M. Yu, T. Feng, M. Tian, R. Chang, Y. Yue, Z. Pan, J. Zhao, X. Li, *ACS Catal.* **2021**, 11, 11016.
- [37] R. Ouyang, J.-X. Liu, W.-X. Li, *J. Am. Chem. Soc.* **2013**, 135, 1760.
- [38] A. González-Garay, M. S. Frei, A. Al-Qahtani, C. Mondelli, G. Guillén-Gosálbez, J. Pérez-Ramírez, *Energy Environ. Sci.* **2019**, 12, 3425.
- [39] X. Hai, S. Xi, S. Mitchell, K. Harrath, H. Xu, D. F. Akl, D. Kong, J. J. Li, Z. Li, T. Sun, H. Yang, Y. Cui, C. Su, X. Zhao, J. J. Li, J. Pérez-Ramírez, J. Lu, *Nat. Nanotechnol.* **2022**, 17, 174.
- [40] Y. Zhai, J. Zhao, X. Di, S. Di, B. Wang, Y. Yue, G. Sheng, H. Lai, L. Guo, H. Wang, X. Li, *Catal. Sci. Technol.* **2018**, 8, 2901.
- [41] I. Platzman, R. Brenner, H. Haick, R. Tannenbaum, *J. Phys. Chem. C* **2008**, 112, 1101.
- [42] M. C. Biesinger, *Surf. Interface Anal.* **2017**, 49, 1325.
- [43] O. Müller, M. Nachtegaal, J. Just, D. Lützenkirchen-Hecht, R. Frahm, *J. Synchrotron Radiat.* **2016**, 23, 260.
- [44] A. H. Clark, P. Steiger, B. Bornmann, S. Hitz, R. Frahm, D. Ferri, M. Nachtegaal, *J. Synchrotron Radiat.* **2020**, 27, 681.
- [45] A. H. Clark, J. Imbao, R. Frahm, M. Nachtegaal, *J. Synchrotron Radiat.* **2020**, 27, 551.
- [46] B. Ravel, M. Newville, *J. Synchrotron Radiat.* **2005**, 12, 537.
- [47] G. Kresse, J. Furthmüller, *Phys. Rev. B* **1996**, 54, 11169.
- [48] G. Kresse, J. Furthmüller, *Comput. Mater. Sci.* **1996**, 6, 15.
- [49] J. P. Perdew, K. Burke, M. Ernzerhof, *Phys. Rev. Lett.* **1996**, 77, 3865.
- [50] S. Grimme, J. Antony, S. Ehrlich, H. Krieg, *J. Chem. Phys.* **2010**, 132, 154104.
- [51] P. E. Blöchl, *Phys. Rev. B* **1994**, 50, 17953.
- [52] G. Kresse, D. Joubert, *Phys. Rev. B* **1999**, 59, 1758.
- [53] G. Makov, M. C. Payne, *Phys. Rev. B* **1995**, 51, 4014.
- [54] M. Álvarez-Moreno, C. de Graaf, N. López, F. Maseras, J. M. Poblet, C. Bo, *J. Chem. Inf. Model.* **2015**, 55, 95.
- [55] A. Ruiz-Ferrando, ioChem-BD Dataset, <https://doi.org/10.19061/iochem-bd-1-260> (accessed: April 2023).
- [56] G. Wernet, C. Bauer, B. Steubing, J. Reinhard, E. Moreno-Ruiz, B. Weidema, *Int. J. Life Cycle Assess.* **2016**, 21, 1218.
- [57] M. A. J. Huijbregts, Z. J. N. Steinmann, P. M. F. Elshout, G. Stam, F. Veronesi, M. Vieira, M. Zipp, A. Hollander, R. van Zelm, *Int. J. Life Cycle Assess.* **2017**, 22, 138.